GPM-Derived Climatology of Attenuation Due to Clouds and Precipitation at Ka-Band

Alessandro Battaglia, Kamil Mroz, Daniel Watters, and Fabrice Ardhuin

***Abstract*— Attenuation from clouds and precipitation hinders the use of Ka-band in SARs, radar altimeters and in satellite link communications. The NASA-JAXA Global Precipitation Measurement (GPM) mission, with its core satellite payload including a dual-frequency (13.6 and 35.5 GHz) radar and a multifrequency passive microwave radiometer, offers an unprecedented opportunity for better quantifying such attenuation effects. Based on four years of GPM products, this article presents a global climatology of Ka-band attenuation caused by clouds and precipitation and analyses the impact of the precipitation diurnal cycle. As expected, regions of high attenuation mirror precipitation patterns. Clouds and precipitation cause two-way attenuation at 35.5 GHz in excess of 3 dB about 1.5% of the time in the regions below 65°, peaking at as much as 10% in the tropical rain belt and the South Pacific Convergence Zone and at circa 5% along the storm tracks of the North Atlantic and Pacific Oceans. Confirming previous findings, the diurnal cycle is particularly strong over the land and during the summer period; while over the ocean, the diurnal cycle is generally weaker some coherent features emerge in the tropical oceans and in the northern hemisphere. Results are useful for estimating data loss from (sun-synchronous) satellite adopting active instruments/links at a frequency close to 35 GHz.**

***Index Terms*— Attenuation, cloud and precipitation, Ka-band, radar.**

I. Introduction

MILLIMETER radars offer unprecedented capabilities in cloud and precipitation and ocean/land remote sensing due to their greater potential for finer resolution and improved sensitivity. In particular, Ka-band frequencies in the range between 26.5 and 40.0 GHz have been increasingly used and proposed for satellite missions and, due to the higher bandwidth they offer, in satellite communication links [1]. The first Ka-band precipitation radar at 35.55 GHz was launched in 2014 as a part of the Global Precipitation Measurement (GPM) mission payload [2]; several mission proposals and notional concepts targeting cloud and precipitation and their dynamics [3]–[6], including Cubesat platforms [7], are based on measurements close to such frequency. Some of the altimeters are currently operated at Ka-band (AltiKa at 35.75 GHz [8]), whereas missions targeting ocean currents (e.g., the SKIM mission [9], [10]) do also envisage the use of the Ka-band Doppler radar; similarly, synthetic aperture radars have been proposed at Ka-band [11], [12] and SWOT is a cross-track SAR interferometer targeted at water level measurements [13].

One of the main drawbacks of the use of the Ka-band is related to the attenuation caused by rain and atmospheric liquid water at such frequencies [14]. At 35.5 GHz, the absorption coefficient (one-way) for cloud water ranges between 0.6 and 1 dB/km/(g/m^3) for temperatures between 25°C and 0°C, respectively; rain is much more efficient than cloud in attenuating Ka radiation (roughly up to a factor of six more when mean mass-weighted diameters exceed 2 mm for the same liquid water amount [14]). For rain, there is an almost linear relationship between one-way attenuation, A_{rain}, and rain rates, RR, of the form [15]

$$A_{\text{rain}}[\text{ dB/km}] = 0.28\ \text{RR [mm/h]}. \tag{1}$$

Similarly, the specific attenuation model for rain at 35.5 GHz proposed by the International Telecommunication Union-Radio Communication Sector (ITU-R) in the Recommendations ITU-R P.838-3 is

$$A_{\text{rain,ITU-R}}[\text{ dB/km}] = 0.34\ (\text{RR [mm/h]})^{0.887}. \tag{2}$$

While such attenuation can be used to retrieve precipitation [15], it is generally detrimental to the altimeter waveform [16], [17] and the SAR images [18] and, thus, causes errors in the retrieval of the geophysical parameters. Due to its nearly global coverage, the NASA-JAXA GPM mission offers a unique opportunity to understand how strongly Ka-band signals are attenuated by weather systems, which areas and seasons are mostly affected, and how the diurnal cycle can modulate such effects.

This article is structured as follows. First, different GPM products used in the study are outlined (see Section II). Second, the global climatology of attenuation due to clouds and precipitation and an analysis of the precipitation diurnal cycle are presented in Section III. Finally, conclusions and future work are summarized in Section IV.

Manuscript received April 8, 2019; revised August 27, 2019; accepted October 20, 2019. Date of publication November 18, 2019; date of current version February 26, 2020. The work of A. Battaglia and K. Mroz was supported by the project Radiation and Rainfall funded by the U.K. National Center for Earth Observation. The work of D. Watters was supported by the Central England NERC Training Alliance. *(Corresponding author: Alessandro Battaglia.)*

A. Battaglia is with the Department of Physics and Astronomy, University of Leicester, Leicester LE1 7RH, U.K., and also with the National Centre for Earth Observation, Leicester LE1 7RH, U.K. (e-mail: a.battaglia@le.ac.uk).

K. Mroz is with the National Centre for Earth Observation, Leicester LE1 7RH, U.K.

D. Watters is with the Department of Physics and Astronomy, University of Leicester, Leicester LE1 7RH, U.K.

F. Ardhuin is with the Ifremer Centre de Bretagne, Laboratoire d'Océanographie Physique et Spatiale, 29280 Plouzané, France.

Color versions of one or more of the figures in this article are available online at http://ieeexplore.ieee.org.

Digital Object Identifier 10.1109/TGRS.2019.2949052

This work is licensed under a Creative Commons Attribution 4.0 License. For more information, see http://creativecommons.org/licenses/by/4.0/

II. GPM Data Set

The GPM mission aims at better understanding the physics underpinning and the spatial and temporal distribution of global precipitation [19]. The mission is a coordinated effort between a "Core Observatory" satellite (launched in 2014) and a constellation of satellites carrying cross track or conically scanning passive microwave radiometers (see [2, Table I] for an updated list). The Core Observatory hosts the Ku- and Ka-bands' dual-frequency precipitation radar DPR) and the GPM microwave imager (GMI), a multifrequency radiometer designed to be the calibration reference standard for the radiometers of the whole constellation. The DPR scans through a 120-km swath at Ka-band and a 245-km swath at Ku-band, while the GMI provides precipitation data on an 885-km-wide swath. A gamut of products is produced from GPM data ranging from instantaneous intercalibrated brightness temperatures to gridded precipitation products (a complete list is provided in [2, Table II]). In this article, three GPM products have been exploited:

1) the Level 2 DPR product, version 05A;
2) the Level 2 GMI-GPROF product, version 05A;
3) the Level 3 IMERG product, version 05A.

The DPR product provides estimates of the Ku- and Ka-bands' path integrated attenuation (PIA) for gases, cloud water, and precipitating hydrometeors. Preliminary to any DPR algorithm, a correction method for attenuation by cloud liquid water and gases is implemented. Such attenuation is calculated by using atmospheric profiles of temperature, pressure, water vapor, and cloud water extracted from the Japanese Meteorological Agency operational analysis (GANAL) for the nonprecipitating areas and the 3.5-km-mesh global Nonhydrostatic ICosahedral Atmospheric Model (NICAM) for precipitating areas, as described in [20]. The estimation of the attenuation caused by the precipitating hydrometeor is based on the surface reference technique (SRT). Note that this includes both the rain and melting snowflakes and precipitating ice. The SRT methodology is thoroughly described in [21], whereas [22] provides an initial assessment of the performance of the different SRTs. PIA estimates are generally more reliable over the ocean because of the more robust modeling of the ocean normalized backscattering cross section and due to a lower surface variability.

There are two products available in the GPM data set for Ka-band PIAs.

1) *The 2A.GPM.DPR Product:* The differential PIA between Ka- and Ku-bands, δPIA(Ka-Ku), is derived by comparing surface returns in and outside the rain area. PIA(Ka) is then computed by assuming a fixed ratio PIA(Ka)/PIA(Ku) = 6.
2) *The 2A.GPM.Ka Product:* PIA(Ka) is directly derived by comparing surface returns inside and outside the rain areas. Note that this product is available both in the normal sensitivity matched scan (KaMS) and in the high sensitivity (KaHS) scans.

An intercomparison between the PIA computed from the DPR and from the KaMS products (see Fig. 1) shows a very good correlation. For the DPR and the KaMS products,

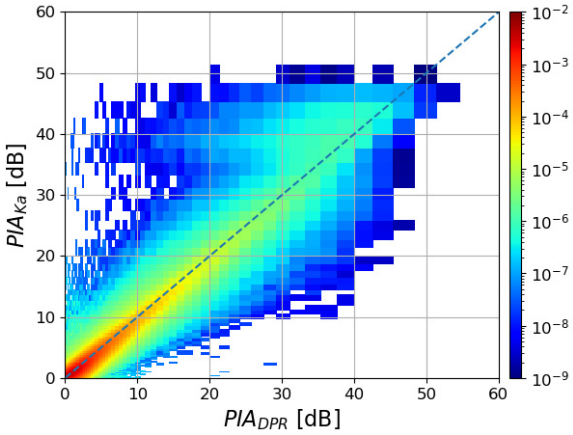

Fig. 1. Scatterplot of the two-way PIA computed from the DPR and from the KaMS products.

the dynamic ranges of both estimates are similar (up to circa 50 dB) since the maximum attenuation is limited by the Ka-band receiver noise (Ka suffers larger attenuation and has less sensitivity). For HS scans, the dynamic range of the PIA(Ka) is about 5 dB better (up to circa 55 dB, not shown) because of the better sensitivity when a longer pulse (1 km) is transmitted. In the following, we have used the first product. The dynamic range depends also on the surface normalized backscattering cross section, which is a strong function of the incidence angle and the surface type. As explained in a previous research [23], [24], PIA estimates based on the SRT are strongly affected by nonuniform-beam-filling effects within the footprint of the radar instruments. Generally, they tend to underestimate the (antenna-averaged) PIA in the presence of highly inhomogeneous rainfall fields. For instance, if half of the beam encounters a PIA of x dB and the other half a PIA of y dB with $x \gg y$, then the PIA estimated by the SRT is approximately $y + 3$ dB and not $0.5(x + y)$ (which is the correct value of the antenna-averaged PIA), where the 3-dB term accounts for the fact that only half of the surface is effectively illuminated by the radar. On the other hand, PIA-SRT is exactly the quantity that is relevant for scatterometers and altimeters in order to quantify the extent to which the surface return is reduced by the atmosphere, and as a result, it is a strong function of the instrument antenna pattern. Therefore, our findings are particularly relevant for all the instruments that have footprints similar to the GPM Ka-radar ($\approx 5 \times 5$ km^2). Instruments with smaller (larger) footprints will tend to produce broader (narrower) probability distribution functions (pdfs) of SRT-based PIAs. Note that for altimeters, the shape of the waveforms in the presence of cloud/precipitation is affected more by the variability of rain within the altimeter footprint than by the mean value of the PIA [25], e.g., patchy rain/cloud cells can distort the waveforms more adversely than heavier but more homogeneous rainfall.

Cloud liquid is also a source of attenuation. The GMI cloud liquid water product [26] is used over ocean where it provides the most reliable estimates of cloud water both in the absence and in the presence of rain. The latter condition is indeed cen-

tral for this study because in that situation, the largest attenuations are expected. Generally, retrieving rain and cloud liquid water path (LWP) simultaneously has proven challenging both from spaceborne [27], [28] and from ground-based remote sensing instruments [29]; as a result, the cloud water content conditional to rain generally depends upon the cloud/rain partitioning assumptions in the algorithm [30]. Note that this is a troublesome area for visible-based algorithms [e.g., the ones used for the Moderate Resolution Imaging Spectroradiometer (MODIS)] as well; such methodologies have deficiencies at large optical thicknesses and past studies suggested that they tend to overestimate the LWP [28], [31]. Over the land, the cloud liquid water product from the combined algorithm [32], which is mainly driven by ancillary environmental data from the Japan Meteorological Agency Global Analysis product, is used. This combined product overestimates cloud water compared to the GMI-only product, and it provides an estimate of the cloud water path only in areas where precipitation is expected.

The third GPM product used in this study is IMERG; it provides a 30-min $0.1^\circ \times 0.1^\circ$ gridded precipitation product from 60°S to 60°N [33]. IMERG is a unified algorithm that combines active and passive microwave measurements from the GPM constellation with infrared measurements from geostationary satellites by using intersatellite calibration, morphing, and neural network techniques. Data from the final run (which performs a monthly gauge adjustment with a latency of three months) of IMERG are used in this study. All GPM products are publicly available at the NASA website (https://pmm.nasa.gov/gpm).

III. Results

A. Global Climatology of Attenuation Due to Clouds and Precipitation

Four years of GPM data have been analyzed, and pdfs for the PIA (all two ways from now onward) caused by the different contributors have been produced at a $1^\circ \times 1^\circ$ resolution. Such gridding corresponds to around 19 000 DPR measurements in the tropics, 25 000 at 55° latitude, increasing to 89 000 at the edge of the swath at $\sim$ 65° latitude each year. An example of the generated pdfs is provided in Fig. 2 for the regions corresponding to the magenta boxes in Fig. 6. From the pdfs of the PIA, any percentile can be computed; for instance, the $97th$ percentiles are shown in Fig. 3. For this high percentile, the effect of gas attenuations is generally of the order of 1 dB and driven by the water vapor amount with largest values typically smaller than 1.4 dB. Cloud attenuations are comparable to gases. Cloudy conditional mean values of liquid water attenuation over the ocean (not shown) generally agree with the results shown in [34, Fig. 5] with cloud water paths peaking at 0.25 kg/m^2 in the Tropics (which roughly correspond to 0.45-dB two ways). Generally (top right), a discontinuity is observed between ocean and land cloud water paths; such gradient is obviously not physical but is dictated by the use of different products; the GMI product over ocean is certainly more trustworthy than that over the land, which is model driven. The cloud PIAs seem to be underestimated

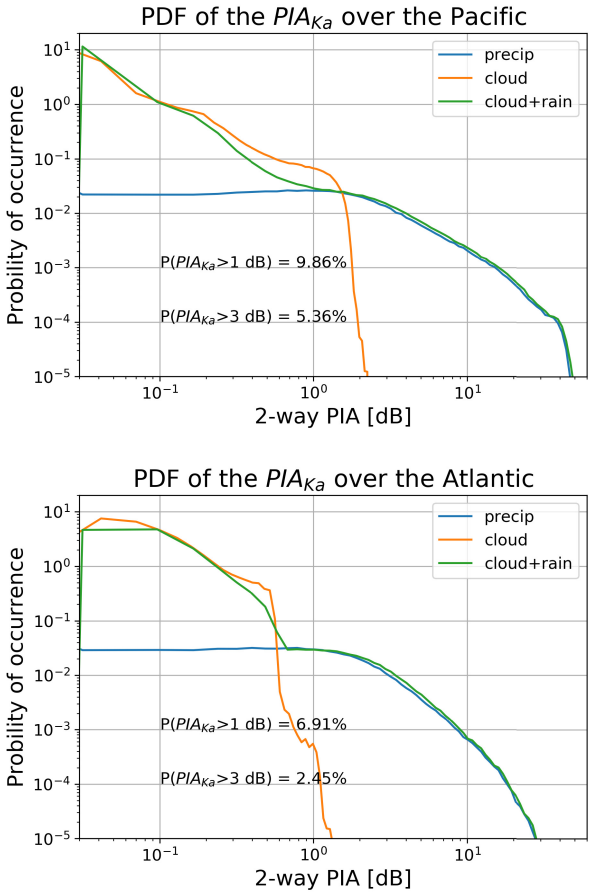

Fig. 2. Pdfs of PIA for cloud, precipitation, and cloud + precipitation for a region in (Top) Central Pacific and (Bottom) North Atlantic as identified by the two black rectangles in Fig. 3.

with respect to the results from [25] where clouds LWPs are derived from MODIS high-resolution (1 km) cloud data. This is particularly acute in the Southern oceans below 40°S and in the tracks of the storms in the northern hemisphere. This may be possibly due to the coarser GMI resolution and to the aforementioned overestimation of the MODIS product.

While the magnitude of the signal from clouds is generally comparable to the gas attenuation (compare the range of values in the top), the signal from precipitation is generally much larger. The geographical distributions over the ocean of the rain PIA (bottom left) mirrors the global precipitation patterns (see [35]), with maxima in the Tropical rain belt, the South Pacific Convergence Zone (SPCZ) extending from the maritime continent south-eastward toward Polynesia and along the storm tracks of the Northern Hemisphere oceans in the mid-latitudes. The $97th$ percentiles are null in several places (where rain occurrences are lower than 3%), and they peak just above 10 dB in the tropical rain belt. When combining rain and clouds (bottom right), the pattern of the $97th$ percentile of PIA does not differ significantly from the rain only image (bottom left), except for approximately 15% increase in the magnitude (see the change in the color bar scale). It shows that the strongest attenuation is observed in the areas of heavy precipitation, and the cloud component additionally enhances the attenuation by several percentages.

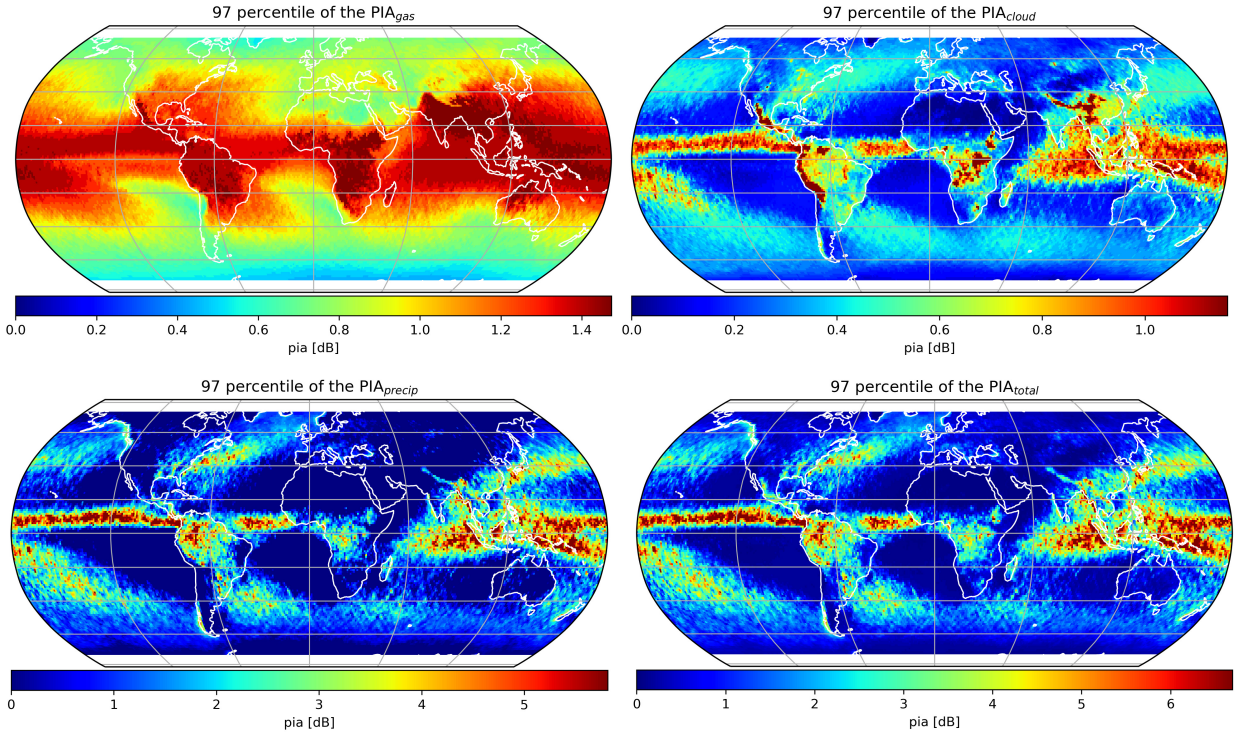

Fig. 3. 97*th* percentile of the two way PIA expressed in dB for (Top Left) gases, (Top Right) clouds, (Bottom Left) precipitation, and (Bottom Right) total (i.e., cloud plus precipitation). A combination of GPM products is used to compute the different contributions. Note that different color scales are used in different plots.

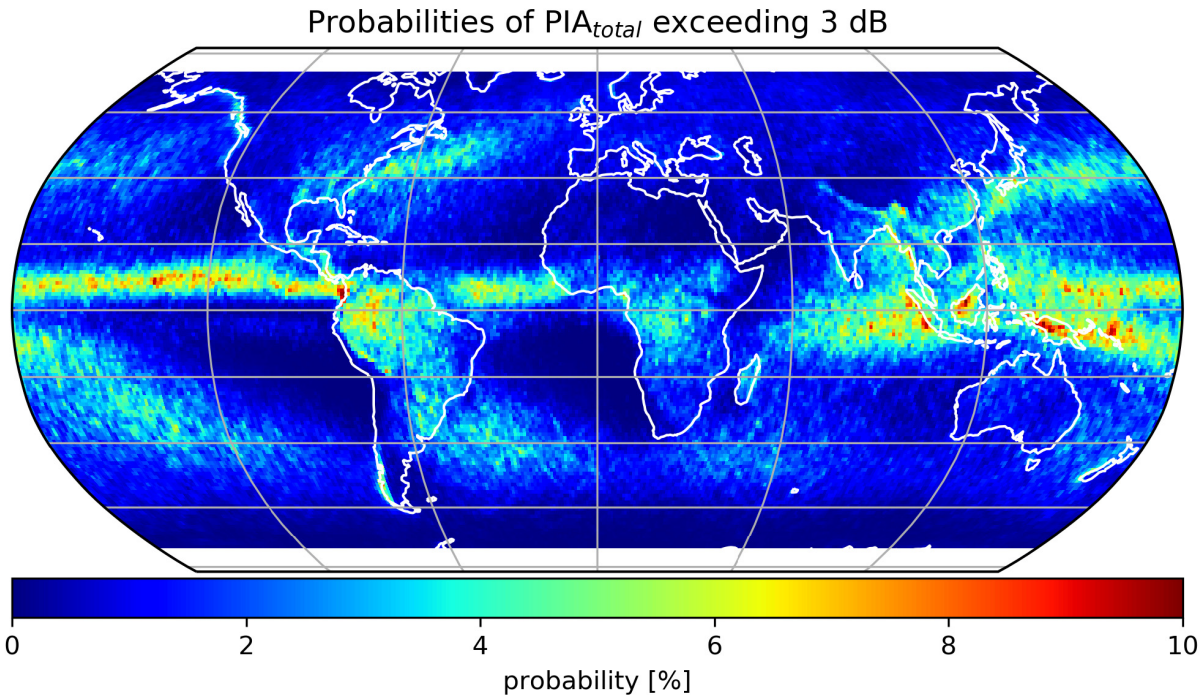

Fig. 4. Probability of the two-way PIA caused by cloud + precipitation exceeding 3 dB derived from combining DPR and GMI measurements.

In Fig. 4, the probabilities of the PIA caused by clouds and precipitation exceeding 3 dB are depicted. The 3-dB level is usually considered detrimental to altimeter waveform measurements, whereas even more stringent thresholds must be imposed for the Doppler scatterometers [10]. On the other hand, for altimeters, the instrument signal-to-noise ratios are generally very large (e.g., the data lost due to rain over the ocean are lower than 0.1% for AltiKa [8]). About 1.5% of data exceed the 3-dB threshold globally, but in the tropical rain belt and the SPCZ, as much as 10% of the surface signals are

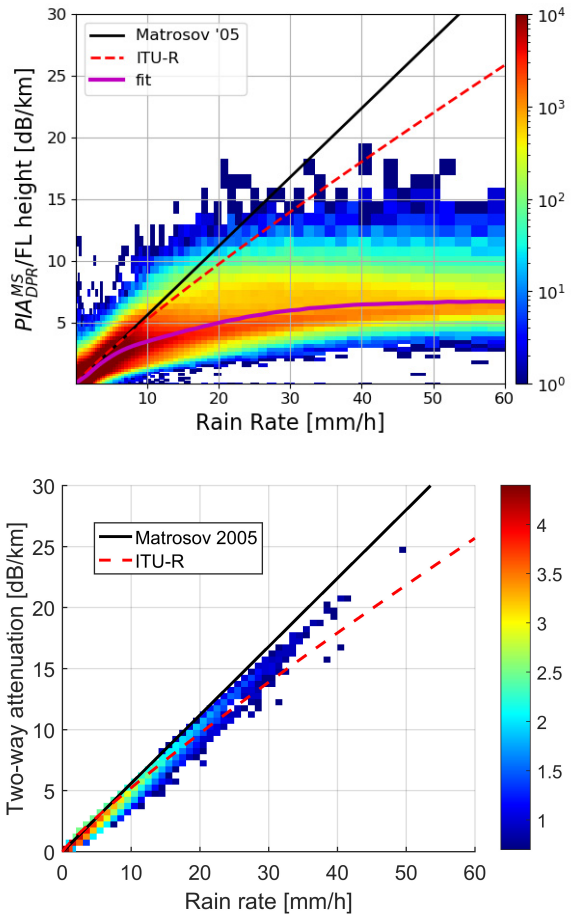

Fig. 5. (Top) Histogram density plot of two-way SRT-PIA rescaled by the height of the freezing level versus the rain rate as derived from the DPR algorithm; the magenta line is the mean of the two-way PIAs for any given rain rate. The back and red lines correspond to the two-way attenuation as derived from the relationship given in (1) and (2), respectively. (Bottom) Rain rate versus two-way attenuation as derived from a data set of disdrometer data (courtesy of Dr. Leo Pio D'Adderio).

expected to be more than halved. Similarly, about 5% of PIAs exceed 3 dB along the storm tracks of the North Atlantic and Pacific Oceans. The spatial patterns shown in Fig. 4 mirror those presented in [25, Fig. 9] based on the Topex/Poseidon rain climatology though their probabilities are slightly higher.

Finally, it is generally interesting to relate the SRT-PIA (rescaled by the height of the freezing level) to the rain rate as derived from the DPR algorithm [see Fig. 5(top)]. The statistical mean relation agrees pretty well with the theoretical curve for PIAs per unit height smaller than 3 dB/km (though with a large noise). Nevertheless, for heavier precipitation, the departure from the linear relationship is more marked with a strong underestimation of SRT-PIA values (see departure between magenta and red lines). As mentioned earlier, nonuniform beam filling is a plausible explanation for such behavior. At medium and high rain rates, therefore, the simple use of the SRT-PIA combined with (1) will obviously lead to a strong underestimation of the rain rate. Another explanation for the large variability of the relationship between attenuation and rain rate could reside in the variability of the drop size distributions. This is, however, ruled out by an extensive analysis of *in situ* measurements of the rain size distributions by the 2-D video disdrometer [36] gathered during field campaigns and from permanent sites of the GPM Ground Validation program. Attenuation coefficients computed by coupling the drop size distribution measurements with extinction cross sections derived from the T-matrix method [37] are presented in Fig. 5(bottom) as a function of rain rate. Clearly, there is not much spread caused by the raindrop size distribution variability.

B. Diurnal Cycle

Another aspect of interest to consider, especially when designing orbits for satellites in sun-synchronous orbits, is the effect of the diurnal cycle on cloud and precipitation that immediately mirrors into an attenuation diurnal cycle. The effects of the diurnal cycle on the water cycle have been thoroughly investigated in the past. Reference [34] investigated the cloud diurnal cycle over the ocean (see [34, Fig. 7]); the strongest cycle occurs mainly in low-cloud coastal regions (with peaks in correspondence to the stratocumuli off the coast of South America and Namibia significantly greater than in their Northern Hemisphere counterparts) with early morning maxima driven mainly by cloud solar absorption [38]. Furthermore, they find that the amplitude of the 24-h harmonic generally tends to decrease when moving toward the open ocean. A significant diurnal cycle is also associated with the maritime continent where it peaks slightly later (10 A.M.), likely connected to sea/land breezes triggering deep convection. Only small diurnal cycles are observed in mid-latitude storms and in correspondence to the tropical deep convective regions over the ocean.

Several studies have discussed the rainfall diurnal cycle as recorded by *in situ* data (i.e., three-hourly weather report and hourly rain-gauge data, e.g., [39]) and by satellite remote sensing instruments [40], [41]. All studies generally agree that: 1) subdaily variability is dominated by the 24-h cycle; 2) the diurnal cycle is driven by frequency rather than intensity; 3) the amplitude of the diurnal cycle is more prominent over the land (and during summer) where a marked minimum in the mid-morning is followed by an afternoon–evening maximum mainly driven by showery and convective precipitation with a significant diurnal cycle amplitude (well exceeding 30% of the daily mean precipitation); 4) over oceans, the amplitude of the 24-h cycle is significantly muted (with values up to 30%) with a peak from midnight to early morning during both winter and summer; 5) there is a weak 12-h cycle over most mid- to high-latitudes land and oceans (with amplitudes lower than 20% and maxima around 5 A.M. and 5 P.M. LST); and 6) in remotely sensed precipitation products, the diurnal cycle resembles that of convective precipitation and is slightly anticipated (≈2 h) compared to that based on the rain-gauge data.

High spatial and temporal resolution satellite precipitation products, such as IMERG, offer an unprecedented opportunity to investigate the diurnal cycle. Reference [42] showed that the 30-min temporal resolution IMERG well captures the diurnal and semidiurnal precipitation patterns identified by

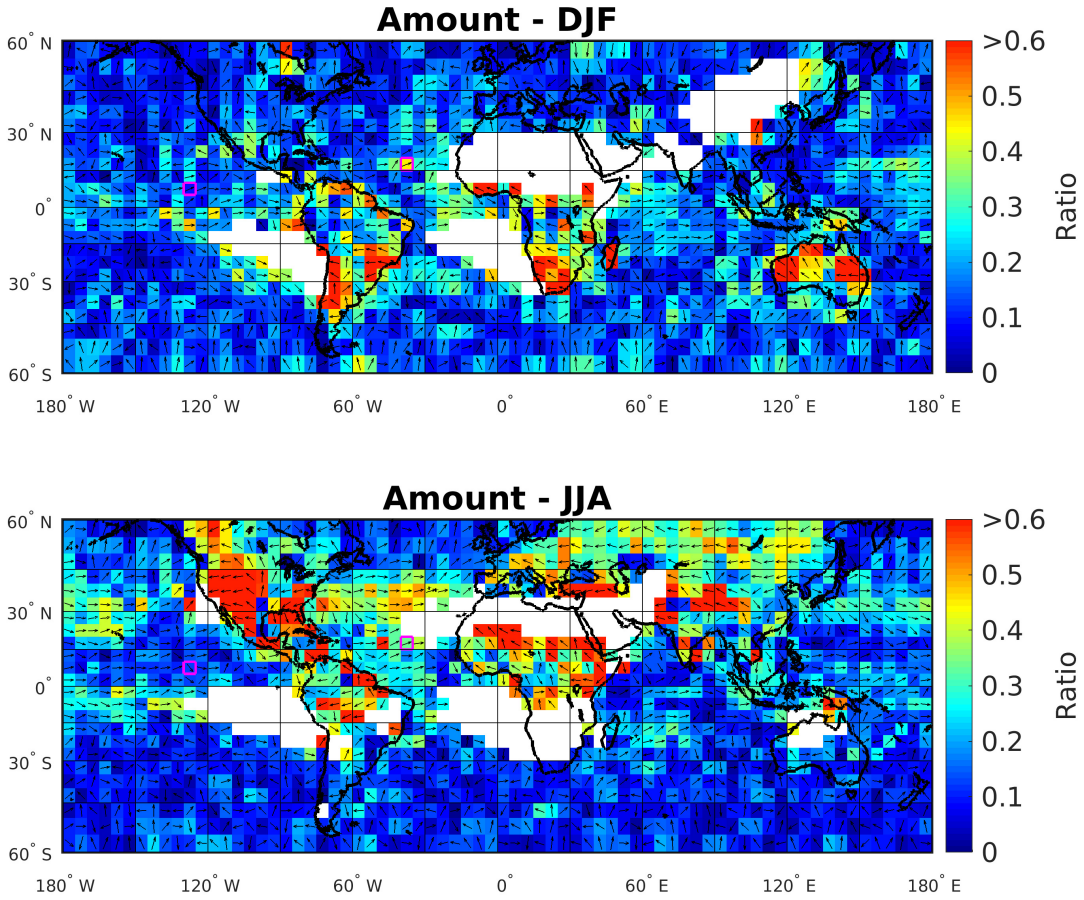

Fig. 6. Diurnal cycles of precipitation amount derived from IMERG. The colors correspond to the ratio of the diurnal harmonic amplitude to the daily mean; the direction of the arrows corresponds to the LST at which the phase peak occurs: North = 00:00, East = 06:00, South = 12:00, and West = 18:00. Statistics for regions with low precipitation amounts (≤100 mm/year) or poor coverage (i.e., lack of estimates at the 5° scale for at least 20% of the diurnal cycle) are not considered. Regions with dark colors are characterized by a marginal diurnal cycle. Magenta-outlined boxes represent the regions selected in Fig. 7.

the ground-based radars over the CONUS during the summer. In a parallel study [43], we have analyzed the diurnal cycle across the globe using four years of IMERG data (June 2014–May 2018); for each 5° lat/lon grid box, precipitation occurrence, amount (mean precipitation, including zero values), and intensity (the conditional mean for precipitation >0 mm/h) have been computed at half-hour resolution. These histograms have been fit by diurnal and semidiurnal harmonic functions with a least-squared-error method [42], weighted by their random errors [43]. The importance of the diurnal and semidiurnal cycles has been then evaluated by looking at the amplitudes of the corresponding harmonics, whereas the position of the maximum in the diurnal harmonic provides the timing of the peak.

The key results of our analysis are summarized in Fig. 6. The strength of the diurnal cycle of precipitation is generally much stronger over the land (cyan to red colors) than over the ocean and during the summer seasons. Note that a 30% ratio of the diurnal harmonic amplitude to the daily mean is indeed a significant signal (i.e., the diurnal harmonic is responsible for a minimum-to-maximum variability equal to 60% of the mean precipitation). Over the land, most of the regions with strong diurnal cycles during summer (e.g., Western plains in U.S., sub-Saharan Africa, South Africa and Madagascar, South Andes, South Brazil, and Paraguay) exhibit a diurnal peak after 18 LST till late evening. Over the ocean, the diurnal cycle is much stronger during the summer. Over the North Atlantic and North Pacific Oceans (bottom), the regions with stronger diurnal cycles are those between 0° and 45°N with maxima that tend to occur in the late-night/early morning up to 6/7 LST with few exceptions close to the continents. In the Southern Oceans (top), the diurnal cycle is generally weaker with maxima clustering toward midnight in the high latitude areas and the late morning (9-12 LST) close to the East and West coasts of the South America continent (but some of these areas have low occurrences of precipitation anyhow). The Tropical oceans within the ITCZ generally feature a weak diurnal cycle but predominantly peaking between 4 and 8 LST. During winter, the diurnal cycle over ocean is much weaker.

C. Diurnal Modulation of the Rain Attenuation

Hourly precipitation data from IMERG can be used to characterize how the attenuation pdfs are modulated by the diurnal cycle. The methodology can be summarized by the following steps.

1) The conditional probability of having rain rates within a certain rain class, RR_k, for a given local time (LST_i),

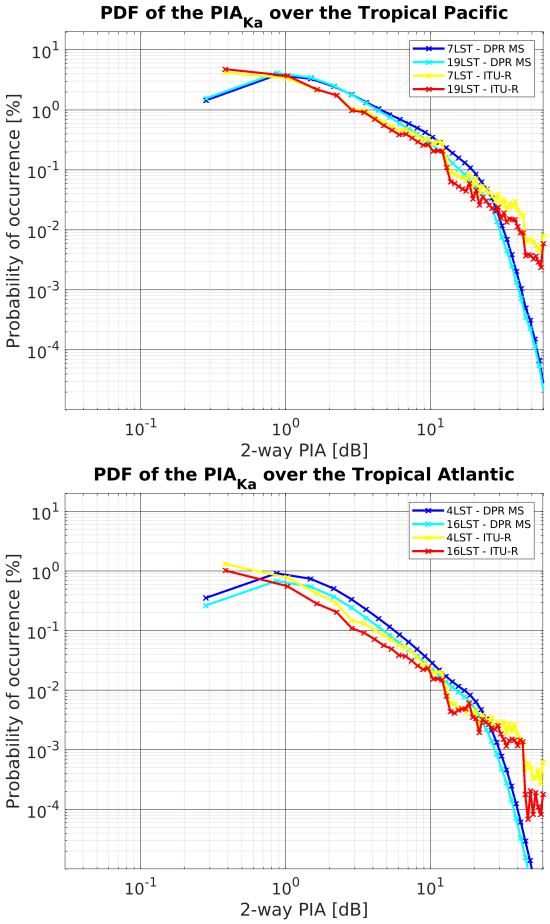

Fig. 7. PDFs s of two-way PIA for the maximum (blue and yellow curves) and minimum (cyan and red curves) of the diurnal cycle derived by using the DPR-MS (blue and cyan curves) and the ITU-R (red and yellow curves) attenuation versus rain rate for a region in (Top) Central Tropical Pacific and in (Bottom) Central Tropical Atlantic. Both regions are highlighted by the magenta boxes in Fig. 6. A freezing level at 4.5 km has been assumed.

$P(\mathrm{RR}_k|\mathrm{LST}_i)$, is constructed from the IMERG product for each location. Note that

$$\sum_k P(\mathrm{RR}_k|\mathrm{LST}_i) = \tilde{P}_{\mathrm{rain}}(\mathrm{LST}_i)$$

the probability of rain at the given LST_i.

2) Rain rates are converted into attenuation by applying an appropriate rain rate versus attenuation relationship. Because of nonuniform-beam-filling, this mapping depends on the observation geometry and sensor characteristics. For a GPM DPR-like instrument, the histogram in Fig. 5(top) can be used to calculate the conditional probability of having attenuation within a certain attenuation class, A_j, for rain rates within the $k-$ class, $P(A_j|\mathrm{RR}_k)$. For sensors with small footprints, the histogram in Fig. 5(bottom) will be more appropriate.
3) The probability of having attenuation within a certain attenuation class, A_j, at a given LST_i is then computed as

$$P(A_j|\mathrm{LST}_i) = \sum_k P(\mathrm{RR}_k|\mathrm{LST}_i)P(A_j|\mathrm{RR}_k). \quad (3)$$

Note that $\sum_j P(A_j|\mathrm{LST}_i) = \tilde{P}_{\mathrm{rain}}(\mathrm{LST}_i)$.

4) The probability of having a certain PIA_j at a given LST_i is then computed as $P(\mathrm{PIA}_j|\mathrm{LST}_i) = P(A_j|\mathrm{LST}_i)$ with $\mathrm{PIA}_j = A_j \times \mathrm{FL}$, where FL is the freezing level height.

Fig. 7 is produced by this methodology for the same regions used in Fig. 2. Results are shown for the maximum and minimum of the diurnal cycle and for two attenuations versus rain-rate relationships: the DPR-MS (blue and cyan) and the ITU-R (red and yellow) corresponding to a ≈5-km footprint and very fine footprint, with the latter clearly producing much larger PIAs. Note that the Tropical Pacific (Atlantic) region exhibits a weak (strong) diurnal cycle with a peak-to-mean rainfall equal to 12.1% (18.0%) of the mean rainfall; precipitation occurrence is 19.5% (2.8%) in the diurnal minimum hour, 19 LST (16 LST), and 20.1% (3.7%) in the diurnal maximum hour, 7 LST (4 LST). The probability of the Ka PIA from the DPR MS exceeding 3 dB in the diurnal maximum hour is 4.8% (0.3%). The curves in the plots for the different LSTs nearly overlap due to the use of a logarithmic scale on the y-axis.

IV. Conclusion

The availability of novel products from the NASA GPM mission offers a unique opportunity for quantifying attenuation effects caused by clouds and precipitation in the proximity of 35.5 GHz (Ka-band). Based on four years of GPM products, this article presents a global climatology of attenuation at Ka caused by clouds and precipitation and analyses the impact of the precipitation diurnal cycle. Based on a combination of measurements from active and passive instruments onboard the GPM Core Observatory, pdfs of integrated attenuation caused by clouds and precipitation have been derived over all latitudes below 65° and at 1° resolution. This provides probabilities for total attenuation exceeding any given threshold (e.g., in this article, we have presented the probability of exceeding the 3-dB threshold). Similarly, the IMERG product with its unprecedented temporal and spatial resolution allows to study the diurnal cycle of precipitation. Since the higher percentiles of attenuation at Ka are dominated by rainy pixels, the combination of both data sets allows for the quantification of the diurnal variability of the attenuation at any location. A methodology to map IMERG pdfs of rainfall into pdfs of attenuation has been described. Results are, therefore, useful for a variety of applications related to quantifying data loss from satellite adopting active instruments/links at frequency close to 35 GHz.

While the new stream of products from the GPM constellation has certainly produced a significant step forward in the monitoring of clouds and precipitation and their attenuation effects, further improvements for the global cloud and precipitation observing system are certainly recommended along the following guidelines.

1) A better quantification of attenuation due to cloud water path over the land must be established. This may require combining microwave and visible sensors.
2) Nonuniform beam filling effects and their detrimental effects on rainfall and on PIA estimates must be mitigated.

3) Better insight about how cloud and rain water paths covary must be gained.

ACKNOWLEDGMENT

This research used the ALICE High Performance Computing Facility at the University of Leicester. Dr. L. Pio D'Adderio has performed the data analysis on the 2DVD data sets that are freely available at https://ghrc.nsstc.nasa.gov/home/field-campaigns.

REFERENCES

[1] T. V. Omotosho, J. S. Mandeep, and M. Abdullahb, "Cloud cover, cloud liquid water and cloud attenuation at Ka and V bands over equatorial climate," *Meteorol. Appl.*, vol. 21, no. 3, pp. 777–785, 2014, doi: 10.1002/met.1417.

[2] G. Skofronick-Jackson *et al.*, "The Global Precipitation Measurement (GPM) mission's scientific achievements and societal contributions: Reviewing four years of advanced rain and snow observations," *Quart. J. Roy. Meteorol. Soc.*, vol. 144, pp. 27–48, Nov. 2018, doi: 10.1002/qj.3313.

[3] J. Leinonen, M. D. Lebsock, S. Tanelli, K. Suzuki, H. Yashiro, and Y. Miyamoto, "Performance assessment of a triple-frequency spaceborne cloud–precipitation radar concept using a global cloud-resolving model," *Atmos. Meas. Tech.*, vol. 8, no. 8, pp. 3493–3517, 2015, doi: 10.5194/amt-8-3493-2015.

[4] P. Joe *et al.*, "The polar precipitation measurement mission," in *Proc. 6th Eur. Conf. Radar Meteorol. Hydrol., Satell. Radar Meas. Hydro-Meteorol. Appl., Sibiu, Romania*, Sep. 2010, pp. 6–10.

[5] A. Battaglia and P. Kollias, "Error analysis of a conceptual cloud Doppler stereoradar with polarization diversity for better understanding space applications," *J. Atmos. Ocean Technol.*, vol. 32, no. 7, pp. 1298–1319, 2014, doi: 10.1175/JTECH-D-14-00015.1.

[6] S. Tanelli *et al.*, "Radar concepts for the next generation of spacebome observations of cloud and precipitation processes," in *Proc. IEEE Radar Conf.*, Oklahoma City, OK, USA, Apr. 2018, pp. 1245–1249.

[7] E. Peral, S. Tanelli, Z. Haddad, O. Sy, G. Stephens, and E. Im, "Raincube: A proposed constellation of precipitation profiling radars in cubesat," in *Proc. IEEE Int. Geosci. Remote Sens. Symp. (IGARSS)*, Milan, Italy, Jul. 2015, pp. 1261–1264, doi: 10.1109/IGARSS.2015.7326003.

[8] N. Steunou, J. D. Desjonquères, N. Picot, P. Sengenes, J. Noubel, and J. C. Poisson, "AltiKa altimeter: Instrument description and in flight performance," *Mar. Geodesy*, vol. 38, pp. 22–42, Oct. 2015, doi: 10.1080/01490419.2014.988835.

[9] F. Ardhuin *et al.*, "Measuring currents, ice drift, and waves from space: The sea surface kinematics multiscale monitoring (SKIM) concept," *Ocean Sci.*, vol. 14, pp. 337–354, 2018, doi: 10.5194/os-14-337-2018.

[10] F. Ardhuin *et al.*, "SKIM, a candidate satellite mission exploring global ocean currents and waves," *Frontiers Mar. Sci.*, vol. 6, p. 209, Apr. 2019, doi: 10.3389/fmars.2019.00209.

[11] M. Ludwig, S. D'Addio, M. Aguirre, J.-C. Angevain, E. Saenz, and K. Engel, "Imaging Ka-band SAR interferometer," in *Proc. 3rd Int. Asia–Pacific Conf. Synth. Aperture Radar (APSAR)*, Sep. 2011, pp. 1–4.

[12] S. Gao *et al.*, "A Ka/X-band digital beamforming synthetic aperture radar for Earth observation," in *Proc. 7th Int. Conf. Recent Adv. Space Technol. (RAST)*, Jun. 2015, pp. 681–686.

[13] R. Morrow *et al.*, "Global observations of fine-scale ocean surface topography with the surface water and ocean topography (SWOT) Mission," *Frontiers Mar. Sci.*, to be published.

[14] R. Lhermitte, "Attenuation and scattering of millimeter wavelength radiation by clouds and precipitation," *J. Atmos. Ocean Technol.*, vol. 7, no. 3, pp. 464–479, 1990.

[15] S. Y. Matrosov, "Attenuation-based estimates of rainfall rates aloft with vertically pointing K_a-band radars," *J. Atmos. Ocean Technol.*, vol. 22, no. 1, pp. 43–54, 2005.

[16] F. M. Monaldo, J. Goldhirsh, and E. J. Walsh, "Altimeter height measurement error introduced by the presence of variable cloud and rain attenuation," *J. Geophys. Res.*, vol. 91, no. C2, pp. 2345–2350, 1986.

[17] P. Bonnefond *et al.*, "The benefits of the Ka-band as evidenced from the SARAL/AltiKa altimetric mission: Quality assessment and unique characteristics of AltiKa data," *Remote Sens.*, vol. 10, no. 1, p. 83, 2018. [Online]. Available: http://www.mdpi.com/2072-4292/10/1/83

[18] F. S. Marzano, S. Mori, and J. A. Weinman, "Evidence of rainfall signatures on X-band synthetic aperture radar imagery over land," *IEEE Trans. Geosci. Remote Sens.*, vol. 48, no. 2, pp. 950–964, Feb. 2010.

[19] G. Skofronick-Jackson *et al.*, "The global precipitation measurement (GPM) mission for science and society," *Bull. Amer. Meteorol. Soc.*, vol. 98, no. 8, pp. 1679–1695, 2016, doi: 10.1175/BAMS-D-15-00306.1.

[20] T. Kubota, M. Satoh, T. Nasuno, S. Seto, T. Iguchi, and R. Oki, "Development of cloud liquid water database using global cloud-system resolving model for GPM/DPR algorithm," in *Proc. IEEE Int. Geosci. Remote Sens. Symp.*, Jul. 2012, pp. 350–353.

[21] T. Iguchi *et al.*, "GPM/DPR level-2 algorithm theoretical basis document," JAXA-NASA, Tech. Rep., 2017. [Online]. Available: https://pps.gsfc.nasa.gov/Documents/ATBD_DPR_201708_whole_1.pdf

[22] R. Meneghini, H. Kim, L. Liao, J. A. Jones, and J. M. Kwiatkowski, "An initial assessment of the surface reference technique applied to data from the dual-frequency precipitation radar (DPR) on the GPM satellite," *J. Atmos. Ocean. Technol.*, vol. 32, no. 1, pp. 2281–2296, Dec. 2015, doi: 10.1175/JTECH-D-15-0044.1.

[23] S. L. Durden, "Relating GPM radar reflectivity profile characteristics to path-integrated attenuation," *IEEE Trans. Geosci. Remote Sens.*, vol. 56, no. 7, pp. 4065–4074, Jul. 2018.

[24] K. Mroz, A. Battaglia, T. Lang, S. Tanelli, and G. F. Sacco, "Global precipitation measuring dual-frequency precipitation radar observations of hailstorm vertical structure: Current capabilities and drawbacks," *J. Appl. Meteorol. Climatol.*, vol. 57, no. 9, pp. 2161–2178, 2018, doi: 10.1175/JAMC-D-18-0020.1.

[25] J. Tournadre, J. Lambin-Artru, and N. Steunou, "Cloud and rain effects on AltiKa/SARAL Ka-band radar altimeter—Part I: Modeling and mean annual data availability," *IEEE Trans. Geosci. Remote Sens.*, vol. 47, no. 6, pp. 1806–1817, Jun. 2009, doi: 10.1109/TGRS.2008.2010130.

[26] C. D. Kummerow *et al.*, "The evolution of the goddard profiling algorithm to a fully parametric scheme," *J. Atmos. Ocean. Technol.*, vol. 32, no. 12, pp. 2265–2280, Dec. 2015.

[27] M. D. Lebsock, T. S. L'Ecuyer, and G. L. Stephens, "Detecting the ratio of rain and cloud water in low-latitude shallow marine clouds," *J. Appl. Meteorol. Climatol.*, vol. 50, no. 2, pp. 419–432, 2011.

[28] J. Leinonen, M. D. Lebsock, G. L. Stephens, and K. Suzuki, "Improved retrieval of cloud liquid water from *CloudSat* and MODIS," *J. Appl. Meteorol. Climatol.*, vol. 55, no. 8, pp. 1831–1844, 2016.

[29] A. Battaglia, P. Saavedra, T. Rose, and C. Simmer, "Characterization of precipitating clouds by ground-based measurements with the triple-frequency polarized microwave radiometer ADMIRARI," *J. Appl. Meteorol. Climatol.*, vol. 49, no. 3, pp. 394–414, 2010, doi: 10.1175/2009JAMC2340.1.

[30] A. Battaglia, P. Saavedra, T. Rose, and C. Simmer, "Rain observations by a multifrequency dual-polarized radiometer," *IEEE Geosci. Remote Sens. Lett.*, vol. 6, no. 2, pp. 354–358, Apr. 2009.

[31] D. Painemal and P. Zuidema, "Assessment of MODIS cloud effective radius and optical thickness retrievals over the Southeast Pacific with VOCALS-REx *in situ* measurements," *J. Geophys. Res., Atmos.*, vol. 116, no. D24, pp. 1–16, 2011.

[32] M. Grecu *et al.*, "The GPM combined algorithm," *J. Atmos. Ocean. Technol.*, vol. 33, no. 10, pp. 2225–2245, 2016.

[33] G. J. Huffman *et al.*, "Algorithm theoretical basis document (ATBD) version 4.6 for the NASA global precipitation measurement (GPM) integrated multi-satellite retrievals for GPM (IMERG)," GPM Project, Greenbelt, MD, USA, Tech. Rep., 2017. Accessed: Feb. 16, 2019.

[34] G. S. Elsaesser, C. W. O'Dell, M. D. Lebsock, R. Bennartz, T. J. Greenwald, and F. J. Wentz, "The multisensor advanced climatology of liquid water path (MAC-LWP)," *J. Climate*, vol. 30, no. 24, pp. 10193–10210, 2017, doi: 10.1175/JCLI-D-16-0902.1.

[35] R. F. Adler, G. Gu, M. Sapiano, J.-J. Wang, and G. J. Huffman, "Global precipitation: Means, variations and trends during the satellite era (1979–2014)," *Surv. Geophys.*, vol. 38, pp. 679–699, Jul. 2017, doi: 10.1007/s10712-017-9416-4.

[36] A. Kruger and W. F. Krajewski, "Two-dimensional video disdrometer: A description," *J. Atmos. Ocean. Technol.*, vol. 19, no. 5, pp. 602–617, 2002.

[37] M. I. Mishchenko, J. W. Hovenier, and L. D. Travis, Eds., *Light Scattering by Nonspherical Particles*. New York, NY, USA: Academic, 2000.

[38] R. Wood, C. S. Bretherton, and D. L. Hartmann, "Diurnal cycle of liquid water path over the subtropical and tropical oceans," *Geophys. Res. Lett.*, vol. 29, no. 23, pp. 7-1–7-4, 2002, doi: 10.1029/2002GL015371.

[39] A. Dai, "Global precipitation and thunderstorm frequencies. Part II: Diurnal variations," *J. Climate*, vol. 14, no. 6, pp. 1112–1128, 2001.

[40] S. W. Nesbitt and E. J. Zipser, "The diurnal cycle of rainfall and convective intensity according to three years of TRMM measurements," *J. Climate*, vol. 16, no. 10, pp. 1456–1475, 2003.
[41] A. Dai, X. Lin, and K.-L. Hsu, "The frequency, intensity, and diurnal cycle of precipitation in surface and satellite observations over low-and mid-latitudes," *Climate Dyn.*, vol. 29, no. 7, pp. 727–744, Dec. 2007.
[42] O. Sungmin and P.-E. Kirstetter, "Evaluation of diurnal variation of GPM IMERG-derived summer precipitation over the contiguous US using MRMS data," *Quart. J. Roy. Meteorol. Soc.*, vol. 144, pp. 270–281, Nov. 2018, doi: 10.1002/qj.3218.
[43] D. Watters and A. Battaglia, "The summertime diurnal cycle of precipitation derived from IMERG," *Remote Sens.*, vol. 11, no. 15, p. 1781, 2019. [Online]. Available: https://www.mdpi.com/2072-4292/11/15/1781

Alessandro Battaglia graduated from the University of Padua, Padua, Italy, with a thesis in particle physics. He received the Ph.D. degree in physics from the University of Ferrara, Ferrara, Italy.

He is experienced in microwave remote sensing of clouds and precipitation with a specific interest in spaceborne radars. He is currently an Associate Professor with the Physics and Astronomy Department, University of Leicester, Leicester, U.K., and the Science Co-Director of the U.K. Center for Earth Observation and Instrumentation. He is also a member of the Precipitation Measuring Mission Science Team and the Mission Advisory Group, ESA-JAXA EarthCARE Mission, and the ESA SKIM mission.

Kamil Mroz received the M.S. degree in mathematics from the University of Bialystok, Bialystok, Poland, in 2010, and the Ph.D. degree from Loughborough University, Loughborough, U.K., in 2014.

In 2015, he joined the National Centre for Earth Observation, Department of Physics and Astronomy, University of Leicester, Leicester, U.K., where he is also a Radiation and Precipitation Scientist. His research interests include liquid and solid precipitation retrievals using microwave remote sensing.

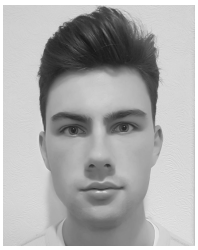

Daniel Watters received the master's degree in physics with a focus on astrophysics from the University of Leicester, Leicester, U.K., where he is currently pursuing the Ph.D. degree with a focus on the Global Precipitation Measurement (GPM) Mission.

He has experience with ground-based and space-borne precipitation radars and satellite.

Fabrice Ardhuin graduated from the École Polytechnique, Palaiseau, France, in 1997. He received the Ph.D. degree in oceanography from the U.S. Naval Postgraduate School, Monterey, CA, USA, in 2001.

He has worked on ocean waves and related topics, from microseisms to remote sensing, with a strong focus on wave–current and wave–ice interactions, first at the French Navy Hydrographic and Oceanographic Service, Brest, France, then Institut Francais de Recherche pour l'Exploitation de la Mer, Plouzané, France, and, recently, CNRS, France. He is currently the Chairman of the Laboratoire d'Océanographie Physique et Spatiale, Plouzané, a member of the SWOT Science Team, and a Principal Investigator of the SKIM Candidate Mission for the ESA Earth Explorer 9.